

High efficient semi-transparent organic solar cell with non-fullerene acceptor: the role of structural parameters on efficiency and transparency

Elmira Annabi Milani

University of Tabriz

Mina Piralaee

University of Tabriz

Sohrab Ahmadi

University of Tabriz

Asghar Asgari (✉ asgari@tabrizu.ac.ir)

University of Tabriz

Article

Keywords: Semi-transparent, organic solar cells, non-fullerene acceptor, ITIC, MoO₃/Ag/MoO₃

Posted Date: May 24th, 2022

DOI: <https://doi.org/10.21203/rs.3.rs-1652328/v1>

License:  This work is licensed under a Creative Commons Attribution 4.0 International License.

[Read Full License](#)

Abstract

Semitransparent organic solar cells are attracted recently because they harvest photons in the near-infrared and ultraviolet range and pass in the visible light region. Semitransparent organic solar cells with ITO/ ZnO/ PBDB-T: ITIC/ MoO₃/Ag/MoO₃ structure have been studied in this work. The effects of active layer thicknesses and the transparent top electrode, MoO₃/Ag/MoO₃, thickness on the solar cell performance such as I-V characteristics, the power conversion efficiency, the average visible transmittance, and the color coordinates in the CIE color space are investigated. The drift-diffusion model, including the density of excitons, and their displacement is used to model the devices. The model is examined with experimentally reported devices, then applied to the new structures. The obtained results are in very good agreement in comparison with experimental data.

Introduction

Solar energy, besides the fusion, has the greatest potential to meet global future needs as one of the main sources of renewable energy. Therefore, harnessing the power of the sun with photovoltaic technologies seems to be the only practical response on a large scale to the energy challenge. On the other hand, organic solar cells (OSCs) have many advantages over conventional inorganic cells and can be easily produced in thin rolls and can bend and flex in a specific structure or even inside clothing. Panels in any desired color can be produced even transparently. It should be noted that, despite the numerous advantages, organic solar cells are still not efficient enough to compete with conventional energy sources, and their large-scale production process for industrial commercialization must be facilitated[1].

Numerous studies have been conducted to improve the power conversion efficiency (PCE), such as the acceptance of solvent additives, applying different active layers, the use of thermal or solvent annealing processes, and the use of triple strategy and reverse structure cells that suggest that shortly and in future developments[2]. In these types of cells, the optical band gap of organic semiconductors can be simply tuned. The thickness of organic active layers in OSC-based photovoltaic technology is about one hundred nanometers which is sufficient to capture photons. Portable mobile chargers, placing batteries on curved surfaces such as car bodies, and even using them in clothing are some of the uses that are anticipated for organic solar cells. Another important property is their flexibility at the wavelength range of absorption spectra. For example, they can be used by adsorption in the infrared region, so, the organic solar cell can be used in car windows, house windows, and any other place that should be transparent. What seems to be a not-so-distant dream is that researchers are trying to make it a reality thanks to transparent solar panels. The basis of semitransparent organic solar cells (ST-OSC) work is to harvest photons in the near-infrared and ultraviolet range and pass them into the visible light region. Once the necessary adjustments have been applied to the ST-OSC structure, acceptable transparency could be attained in the visible region (VR) of the solar spectrum, while it would absorb the NIR region.

To fabricate an ST-OSC, the light absorption inside the active layer must be precisely adjusted to transmit sufficient visible light[3], [4]. In addition, both electrodes must be transparent. There are several ways to

fabricate transparent electrodes. Carbon nanotubes are suitable candidates because they are both cheaper to produce and have good mechanical flexibility[5]. Another carbon-based solution, graphene, has also been studied and used as the top and bottom electrode in semi-transparent organic solar cells. However, these electrodes have low conductivity and require additional chemical doping[6], [7]. Single or multiple pairs of one-dimensional photonic crystals can also be used as the top electrode to achieve an efficiency of about 5–6% in the average visible transmittance (AVT) of 25%, of which deposition of multiple layers of metal oxide (MoO_3 or WO_3) /LiF pairs is necessary[8], [9]. Numerous reports have indicated that at least 25% AVT is required for window applications[10].

Another possible choice for the upper electrode is the dielectric/metal/dielectric (D/M/D) structure. Due to its relatively simple construction and simple fabrication technique, it is more useful in comparison to the alternative approaches such as photonic crystals or graphene-based electrodes[11]. These electrodes have been used in this study. Cell transfer can also be used to calculate the color rendering index (CRI).

Another significant issue in achieving high efficiency in a device is engineering to select the appropriate material to use as the active layer of OSC. Recently, non-fullerene small molecule acceptors have appeared in OSCs as a viable alternative to conventional fullerene acceptors as electron collectors[12]–[15].

The reason for the superior performance of non-fullerene OSCs is the enhanced optical and electronic properties of non-fullerene receptors, as a result of easy adjustment of molecular energy levels[16], [17], superior optical absorption properties[18], the easy synthesis of these materials and therefore low manufacturing costs. Compared to fullerene acceptors[19], [20], these useful features have accelerated the improved performance exhibited by OSCs over the past few years. For example, the non-fullerene acceptor ITIC has shown particularly promising results. This novel small molecule material has a high lying LUMO level (-3.78 eV), which leads to high open-circuit voltage (V_{oc})[21]. and when coupled with a new polymer (PBDB-T), the efficiency is recorded to be more than 11%[22].

In this work, we have theoretically studied and modeled the role of using PBDB-T: ITIC non-fullerene material in semi-transparent solar cell architecture and considered the effects of the active layer and D/M/D layer thickness on the performance parameters and also AVT of the device.

Method And Material

The studied structure used for this study, schematically shown in Fig. 1, is the same as the device reported in Ref[23] with ITO/ ZnO/ PBDB-T: ITIC/ MoO_3 / Ag/ MoO_3 structure, but with a different active layer and D/M/D layers' thickness. Where MoO_3 / Ag/ MoO_3 acts as the transparent top electrode, the inner MoO_3 layer also acts as the hole transport layer. Sol-gel processed ZnO layer is used as the electron transport layer and ITO is the transparent bottom electrode.

The combination of PBDB-T and ITIC in the opaque blend structure has previously shown good photovoltaic performance with more than 11% PCE[21]. When it was employed in the semitransparent

(ST) structure (Fig. 1a), PCE > 7% was achieved at 25% AVT.

To calculate the device's performance parameters such as short-circuit current, J_{sc} , open-circuit voltage, V_{oc} , fill-factor, FF, and power conversion efficiency, PCE, we used the drift-diffusion model, where, in addition to considering the density of excitons, their displacement is taken into account. The used model is extensively explained in our previous publications[24].

To model the device transparency, the transmittance of all layers, and the whole device, $T(\lambda)$, are calculated using the Transfer-Matrix Method, TMM[25]. The transparency properties of the device are determined by both average visible transmittance, AVT, and by transmittance characteristics in the visible light wavelength range (370–740 nm), taking into account the photopic response of the human eye $V(\lambda)$. The AVT value is calculated as follows[26], [27]:

$$AVT = \frac{\int_{370\text{ nm}}^{780\text{ nm}} S_{AM1.5G} T(\lambda) V(\lambda) d\lambda}{\int_{370\text{ nm}}^{780\text{ nm}} S_{AM1.5G} V(\lambda) d\lambda} \quad (1),$$

where $S_{AM1.5}(\lambda)$ is the photon flux under AM 1.5G illumination and $V(\lambda)$ is the photopic response of the human eyes. AVT value of 25% is an acceptable criterion for window applications where it depends on the devices' working circumstances[28]. As the window transparency depends on the response of the human eye, so, the color coordinates (x, y) in the CIE 1931 chromaticity diagram will be another important characteristic of the semi-transparent solar cells calculated using the Eq. 2 [3]:

$$x = \frac{X_1}{\sum_{i=1}^3 X_i}, \quad y = \frac{X_2}{\sum_{i=1}^3 X_i} \quad (2),$$

where $X_i = \int_{370\text{ nm}}^{780\text{ nm}} S_{AM1.5G}^{D65} T(\lambda) \mathfrak{R}_i(\lambda) d\lambda$, and $S_{AM1.5G}^{D65}$ is the CIE standard D65 illuminant spectrum, and the terms $\mathfrak{R}_i(\lambda)$ are color-matching functions defined by the CIE protocol ($X + Y + Z = 1$).

Results And Discussion

This work has studied the introduced devices with different active layer thicknesses and various D/M/D thicknesses. The thicknesses of active layers are 53, 59, 72, 91, 100, 114, 143 nm, and DMD (Top contact) thickness are 10 (nm)/ d_m /30(nm) with d_m : 4, 6, 8, 10, 12, 14, 16 nm. We first examined our model's accuracy in comparison with experimental data reported for the device in Ref.[29], in which the D/M/D thickness is fixed to 10nm/6nm/30nm, and active layer thickness varies from 53nm to 143 nm. As shown in Figs. 2–4, the obtained results are in very good agreement with the experimental results. The characteristics parameters are listed in Table 1. To model the ST-OSC's performances, one has to know the absorption coefficient for the structures. For this purpose, we calculated the absorption coefficient and fitted it to the absorption coefficient reported experimentally in percent. The fitted relation has presented in Eq. 3:

$$\alpha_L \approx \left(\frac{(-37.12 + 100\lambda) + (0.97 - 3e6\lambda + 2.85e12\lambda^2)L}{(-37.12 + 100\lambda) + (0.97 - 3e6\lambda + 2.85e12\lambda^2)L_0} \right) \times \alpha_{L_0}; \quad (3)$$

where λ is the wavelength, and L , and L_0 are the active layer thicknesses. Knowing the absorption coefficient, α_{L_0} , in a thickness such as L_0 , one can find the absorption coefficient for any other thicknesses.

Figure 2 shows the J-V curve of the devices with structure of ITO/ ZnO/ PBDB-T: ITIC/ MoO₃/ Ag/ MoO₃, with fixed thickness of D/M/D in 10nm/6nm/30nm, and PBDB-T: ITIC active layer thickness is: a) 53, b) 59, c) 72, d) 91, e) 100, f) 114, g) 143 nm. It is clear from the figures, that there is very good agreement between our model and experimental results. This figure indicates that all devices have the same V_{oc} , which is close to 0.85 V. This value is ~0.2 V higher than devices containing traditional fullerene receptors, due to the high LUMO of non-fullerene acceptors[21]. This is a major factor that helps to improve the photovoltaic performance of this material system. As the active layer thickness was increasing, the J_{sc} also is increasing.

Table 1
Parameters used in the calculation for the device modeling.

Parameter	value
N_A (1/cm ³)	5e25
N_D (1/cm ³)	5e25
N_c (1/cm ³)	8e27
N_v (1/cm ³)	8e27
Electron Lifetime(s)	8.5e-6
Hole Lifetime(s)	7.5e-6
$V_{built-in}$ (eV)	1.14
Mobility (electron, hole)	variable

The transmittance spectrum of the ST-OSC for different active layer thicknesses is calculated and compared with those experimental data. The transmittance spectrum of the ST-OSC with an active layer of 100nm is presented in Fig. 3a, as an example. The figure shows the experimental transmittance for whole devices, besides, the calculated transmittance of the: MoO₃/Ag/MoO₃ anode, ITO and ZnO compact layer, the active layer, and the whole device. Moreover, for a better understanding of the device's

semi-transparency, AM1.5 spectral irradiance, $S_{AM1.5}(\lambda)$, and $S_{AM1.5}(\lambda) * V(\lambda)$ are demonstrated. It can be seen that there is a good agreement between the obtained transparency for the device and the experimental data. Also, the error bar is included which shows the model's accuracy. In the wavelengths of FWHM of $S_{AM1.5}(\lambda) * V(\lambda)$, the ITO and ZnO compact layer has more than 85% transparency, and the MoO3/Ag/MoO3 anode transparency is about 60–75%, and active layer transparency is about 35% ~ 50%.

In Fig. 3b, the calculated transmittance of the ST-OSC for different active layers thickness is presented. As shown in the figure, the transmittance of the ST-OSC with thin active layers thickness (53–72 nm) is higher than 25% at all wavelengths of FWHM of $S_{AM1.5}(\lambda) * V(\lambda)$, which makes it much suitable for widow application. By exceeding the increment of the active layer thickness, the transmittance of the ST-OSC decreases, whereas, for a longer wavelength, it decreases to less than 25%. However, the AVT of the solar cells in the visible region (370–740 nm) of the devices with active layer thickness thinner than 100 nm is higher than 25% and still suitable for widow application.

In Table. 2, we compared the parameters of the solar cell such as short-circuit current, open-circuit voltage, FF, PCE, and AVT of the modeled devices with experimental data[23]. As expected, with increasing the thickness of the active layer, the absorption increases, and consequently PCE increases. In contrast, the fill factor (FF) declined with increasing active layer thickness. Although the J_{sc} is highest for the active layer with a thickness of 143 nm, the FF is low and is 49.6%. The decrease in FF is associated with an increase in recombination, consequently an increase in series resistance and a decrease in shunt resistance values. Optimum PCE is obtained at an active layer thickness of 100 nm with a maximum PCE value of 9.32%. To the best of our knowledge, this PCE is one of the few reported PCEs with more than 7% for a single-junction semitransparent OSC.

Table 2
The model devices' essential parameters compared to experimental data [23].

Thickness (nm)	J_{sc} (mA/cm ²)		V_{oc} (V)		FF (%)		PCE (%)		AVT(%)	
	Th.	Exp.	Th.	Exp.	Th.	Exp.	Th.	Exp.	Th.	Exp.
53	7.33	6.85	0.853	0.884	59.50	66.5	4.79	4.2	33.5	35.3
59	8.94	8.41	0.86	0.89	63.95	66.9	6.4	5.2	32.0	33
72	9.5	8.75	0.863	0.897	54.75	63.2	5.66	5.01	28.8	31.1
91	13.30	12.62	0.867	0.87	59.57	59.4	8.81	6.8	23.6	26.6
100	14.28	13.8	0.867	0.886	59	59	9.32	7.4	21.5	25.2
114	14.76	15.08	0.854	0.87	55.51	51.5	9.02	6.8	18.3	23.2
143	15.14	13.82	0.854	0.89	49.41	49.2	8.21	6.3	14.7	20.2

As can be seen from the Table. 2, and Fig. 4, The PCE increases with increasing active layer thickness until it reaches a maximum value at the thickness of 100 nm. For thicknesses thicker than 100nm, PCE is reduced due to the decreasing of FF. Unlike the PCE, the AVT decreases linearly with increasing active layer thickness. For the devices that can be used as a window, the device with an active layer of 100 nm has the highest PCE.

It is well known that organic thin-film solar cells act as multilayer optical cavities in which the distribution of the optical field is governed by the effect of optical interference, due to the reflection of the incident light at the layer interfaces [30]. In the studied devices, the D/M/D top contact which includes 3 layers can be an important layer for optical interference. To find out the effects of D/M/D layers on the device performance, D/M/D (6nm/ d_m /40nm) layers with different thicknesses of the metal layer, ' d_m ', have been analyzed. For this purpose, each reported device in Table 2, with fixed active layer thickness has been studied using different metal thicknesses in the D/M/D layer, d_m . We have calculated all performance parameters such as the J-V curve, EQE, T, and AVT. As an example, for the devices with the active layer thickness of 53 nm, and d_m : 4, 6, 8, 10, 12, 14, 16 (nm), the performance parameters are presented in Fig. 5. As shown in Fig. 5a, with increasing the metal thickness, J_{SC} increases, but the V_{OC} does not change. In these devices, the exciton generation rate depends on the optical field intensity which is located close to the anode/active layer interface when light enters through the D/M/D electrode under top illumination[31]. So, the ' d_m ' thickness changes can dominantly affect the J_{SC} values. Fig. 5b shows the EQE of the devices as a function of wavelengths, in which the highest EQE value belongs to thick ' d_m ', $d_m=16$ nm. For all devices, the transmittance is higher than 25% for most visible wavelengths (Fig. 5c). Finally, Fig. 5d shows the AVT of the devices as a function of ' d_m ' thickness. The AVT of all devices is higher than 36% and the maximum AVT is obtained for $d_m=6$ nm. So, all devices can be used in the windows application.

All performance parameters for the device are presented in Table. 3. As depicted in the table, all devices are practical for the window application with different PCE, while the highest value for PCE is for $d_m=16$ nm. Also, the highest AVT was achieved for $d_m=6$ nm, with 3.11% PCE.

Table 3
The performance parameters for the device with an active layer thickness of 53 nm.

d_m (nm)	J_{SC} (mA/cm ²)	FF(%)	V_{oc} (V)	PCE(%)	AVT(%)
4	5.55	55.49	0.82	3.27	45.40
6	5.35	54.66	0.82	3.11	46.27
8	5.36	54.60	0.82	3.10	46.00
10	5.58	55.28	0.82	3.28	44.59
12	6.70	57.86	0.84	4.19	42.49
14	5.96	55.68	0.84	3.59	39.61
16	6.74	57.98	0.84	4.22	36.48

In Fig. 6, we have presented the J-V curves of the devices with different active layer thicknesses and various d_m thicknesses. The figure shows that any change in d_m thickness doesn't change the V_{OC} values. The J_{SC} increases with increasing d_m and reaches 14.88 mA/cm² for the sample with an active layer thickness of $d_m=16$ nm, where the fill factor is the lowest value (46%-48%) in comparison with other samples. From the point of view of the fill factor, the sample with $d_m= 16$ nm and the active layer of 59nm has the maximum FF, 70.49%.

In Fig. 7, the devices' J_{SC} , FF, and PCE are presented as a function of ' d_m ' thickness and for various active layer thicknesses. As shown in the figure, for any fixed active layer thickness, with increasing ' d_m ', the J_{SC} is increasing slightly, and the FF is almost constant, so, the PCE increases slightly. With increasing the thickness of active layers for any fixed ' d_m ', the J_{SC} is increasing, and the FF hasn't any certain functionality, then, the PCE increases and reaches a maximum, decreases. The maximum value of PCE happens for samples with an active layer of about 100 nm. For devices with a thicker active layer (more than 100 nm), the FF was lower due to the increase in series resistance, which could be due to the distorted distribution of exciton generation within the active layer (most excitons are generated near the anode/active layer interface) and subsequent carrier transport towards respective electrodes.

To show the applicability of the studied devices in the windows application, the AVT values of the devices are shown in Fig. 8. By increasing the active layer thicknesses, the AVT is increasing, then decreases almost linearly. The maximum value for the AVT belongs to the ST-OSC with the active layer thicknesses of 59nm (see Fig. 7c). As shown in the figure, for a fixed active layer thickness, the AVT value has a maximum at $d_m=6$ nm, then with increasing the d_m value, the AVT decreases. The figure shows that all devices with different d_m and active layer thicknesses thicker than 114 nm deserve semitransparent solar cell conditions.

The CIE color space, including the coordinates of ST-OSC consisting of different active layer thicknesses and different ' d_m ', is shown in Fig. 9. The color coordinates of translucent OSCs with an active layer thickness of about 90–100 nm are located close to the color point or so-called "white dot" in the CIE chromaticity diagram. Proximity indicates that there is a good achromatic or neutral color sensations when looking through devices under AM1.5G illumination. Hence, these devices can transmit high-quality light with near white sensation to the human eye without changing the original color of an object. However, as the thickness of the active layer changes, the color coordinates move in different directions from the white dot. Also, the coordinates are sensitive to d_m values, and both coordinates x and y increase with increasing d_m (see the inset of Fig. 9). For a device with the best PCE and AVT, the thickness of the active layer is 100 nm and the color coordinates are slightly away from the achromatic point, however, the device does not alter the transmitted light by a large extent.

Conclusion

Semitransparent organic solar cells with an active layer of PBDB-T: ITIC and the top transparent electrode of D/M/D are studied. The effects of active layer thicknesses and Ag layer thickness in the top electrode on the solar cell performance are achieved. The results show that the devices with active layer thicknesses of thinner than 100 nm can be used as ST-OSCs, but thinner devices have higher AVT. For the devices with AVT higher than 25%, the devices with an active layer thickness of 100 nm have the highest PCE. For devices with fixed active layer thicknesses, the increasing of metal thickness in D/M/D layers decreases the AVT and increases the PCE. For all devices which have an AVT of more than 25%, the devices with an active layer thickness of 100nm and metal layer thickness of 8 nm have optimum PCE, also, the color coordinates of these devices are close to the achromatic point.

Declarations

Data availability:

The datasets used and/or analysed during the current study available from the corresponding author on reasonable request.

References

1. P. Ray, "Renewable energy and sustainability," *Clean Technol. Environ. Policy*, vol. 21, no. 8, pp. 1517–1533, 2019.
2. F. Zhao *et al.*, "Single-Junction Binary-Blend Nonfullerene Polymer Solar Cells with 12.1% Efficiency," *Adv. Mater.*, vol. 29, no. 18, pp. 1–7, 2017.
3. M. B. Upama *et al.*, "High performance semitransparent organic solar cells with 5% PCE using non-patterned MoO₃/Ag/MoO₃ anode," *Curr. Appl. Phys.*, vol. 17, no. 2, pp. 298–305, 2017.

4. M. B. Upama *et al.*, "Optical modelling of P3HT:PC71BM semi-transparent organic solar cell," *Opt. Quantum Electron.*, vol. 49, no. 1, pp. 1–6, 2017.
5. I. Jeon, C. Delacou, A. Kaskela, E. I. Kauppinen, S. Maruyama, and Y. Matsuo, "Metal-electrode-free Window-like Organic Solar Cells with p-Doped Carbon Nanotube Thin-film Electrodes," *Sci. Rep.*, vol. 6, no. April, pp. 1–2, 2016.
6. Z. Liu, J. Li, Z. H. Sun, G. Tai, S. P. Lau, and F. Yan, "The application of highly doped single-layer graphene as the top electrodes of semitransparent organic solar cells," *ACS Nano*, vol. 6, no. 1, pp. 810–818, 2012.
7. Y. Shi, K. K. Kim, A. Reina, M. Hofmann, L. J. Li, and J. Kong, "Work function engineering of graphene electrode via chemical doping," *ACS Nano*, vol. 4, no. 5, pp. 2689–2694, 2010.
8. G. Xu *et al.*, "High-Performance Colorful Semitransparent Polymer Solar Cells with Ultrathin Hybrid-Metal Electrodes and Fine-Tuned Dielectric Mirrors," *Adv. Funct. Mater.*, vol. 27, no. 15, pp. 1–10, 2017.
9. W. Yu, X. Jia, M. Yao, L. Zhu, Y. Long, and L. Shen, "Semitransparent polymer solar cells with simultaneously improved efficiency and color rendering index," *Phys. Chem. Chem. Phys.*, vol. 17, no. 37, pp. 23732–23740, 2015.
10. K. S. Chen, J. F. Salinas, H. L. Yip, L. Huo, J. Hou, and A. K. Y. Jen, "Semi-transparent polymer solar cells with 6% PCE, 25% average visible transmittance and a color rendering index close to 100 for power generating window applications," *Energy Environ. Sci.*, vol. 5, no. 11, pp. 9551–9557, 2012.
11. W. Yu *et al.*, "Highly efficient semitransparent polymer solar cells with color rendering index approaching 100 using one-dimensional photonic crystal," *ACS Appl. Mater. Interfaces*, vol. 7, no. 18, pp. 9920–9928, 2015.
12. Z. Zheng *et al.*, "Efficient Charge Transfer and Fine-Tuned Energy Level Alignment in a THF-Processed Fullerene-Free Organic Solar Cell with 11.3% Efficiency," *Adv. Mater.*, vol. 29, no. 5, pp. 3–8, 2017.
13. J. Huang *et al.*, "Highly Efficient Organic Solar Cells Consisting of Double Bulk Heterojunction Layers," *Adv. Mater.*, vol. 29, no. 19, 2017.
14. H. Yao *et al.*, "Achieving Highly Efficient Nonfullerene Organic Solar Cells with Improved Intermolecular Interaction and Open-Circuit Voltage," *Adv. Mater.*, vol. 29, no. 21, pp. 1–8, 2017.
15. S. Chen *et al.*, "An All-Solution Processed Recombination Layer with Mild Post-Treatment Enabling Efficient Homo-Tandem Non-fullerene Organic Solar Cells," *Adv. Mater.*, vol. 29, no. 6, pp. 1–7, 2017.
16. Y. Zhang, X. Guo, B. Guo, W. Su, M. Zhang, and Y. Li, "Nonfullerene Polymer Solar Cells based on a Perylene Monoimide Acceptor with a High Open-Circuit Voltage of 1.3 V," *Adv. Funct. Mater.*, vol. 27, no. 10, 2017.
17. Suman, V. Gupta, A. Bagui, and S. P. Singh, "Molecular Engineering of Highly Efficient Small Molecule Nonfullerene Acceptor for Organic Solar Cells," *Adv. Funct. Mater.*, vol. 27, no. 2, 2017.
18. Y. Qin *et al.*, "Highly Efficient Fullerene-Free Polymer Solar Cells Fabricated with Polythiophene Derivative," *Adv. Mater.*, vol. 28, no. 42, pp. 9416–9422, 2016.

19. S. Li *et al.*, "Energy-Level Modulation of Small-Molecule Electron Acceptors to Achieve over 12% Efficiency in Polymer Solar Cells," *Adv. Mater.*, vol. 28, no. 42, pp. 9423–9429, 2016.
20. S. Holliday *et al.*, "High-efficiency and air-stable P3HT-based polymer solar cells with a new non-fullerene acceptor," *Nat. Commun.*, vol. 7, pp. 1–11, 2016.
21. W. Zhao *et al.*, "Fullerene-Free Polymer Solar Cells with over 11% Efficiency and Excellent Thermal Stability," *Adv. Mater.*, vol. 28, no. 23, pp. 4734–4739, 2016.
22. Y. Min, J. Huh, and W. Ho, "Solar Energy Materials & Solar Cells Optimization of thickness and morphology of active layer for high performance of bulk-heterojunction organic solar cells," vol. 94, pp. 1118–1124, 2010.
23. M. B. Upama *et al.*, "High-Efficiency Semitransparent Organic Solar Cells with Non-Fullerene Acceptor for Window Application," *ACS Photonics*, vol. 4, no. 9, pp. 2327–2334, 2017.
24. M. Piralaee and A. Asgari, "Bimetallic core–shell nanoparticles to improve the absorption of P3HT: PCBM organic solar cell," *Appl. Opt.*, vol. 60, no. 29, p. 9087, 2021.
25. T. G. Mackay and A. Lakhtakia, *The Transfer-Matrix Method in Electromagnetics and Optics*, vol. 1, no. 1. 2020.
26. Ç. Çetinkaya *et al.*, "Design and fabrication of a semi-transparent solar cell considering the effect of the layer thickness of MoO₃/Ag/MoO₃ transparent top contact on optical and electrical properties," *Sci. Rep.*, vol. 11, no. 1, pp. 1–18, 2021.
27. Z. Hu *et al.*, "A critical review on semitransparent organic solar cells," *Nano Energy*, vol. 78, no. September, p. 105376, 2020.
28. V. V. Brus, J. Lee, B. R. Luginbuhl, S. J. Ko, G. C. Bazan, and T. Q. Nguyen, "Solution-Processed Semitransparent Organic Photovoltaics: From Molecular Design to Device Performance," *Adv. Mater.*, vol. 31, no. 30, pp. 1–26, 2019.
29. C. Yang, D. Liu, M. Bates, M. C. Barr, and R. R. Lunt, "How to Accurately Report Transparent Solar Cells," *Joule*, vol. 3, no. 8, pp. 1803–1809, 2019.
30. J. Ham, S. Kim, G. H. Jung, W. J. Dong, and J. L. Lee, "Design of broadband transparent electrodes for flexible organic solar cells," *J. Mater. Chem. A*, vol. 1, no. 9, pp. 3076–3082, 2013.
31. B. Joseph, T. Pogrebnaya, and B. Kichonge, "Semitransparent Building-Integrated Photovoltaic: Review on Energy Performance, Challenges, and Future Potential," *Int. J. Photoenergy*, vol. 2019, 2019.

Figures

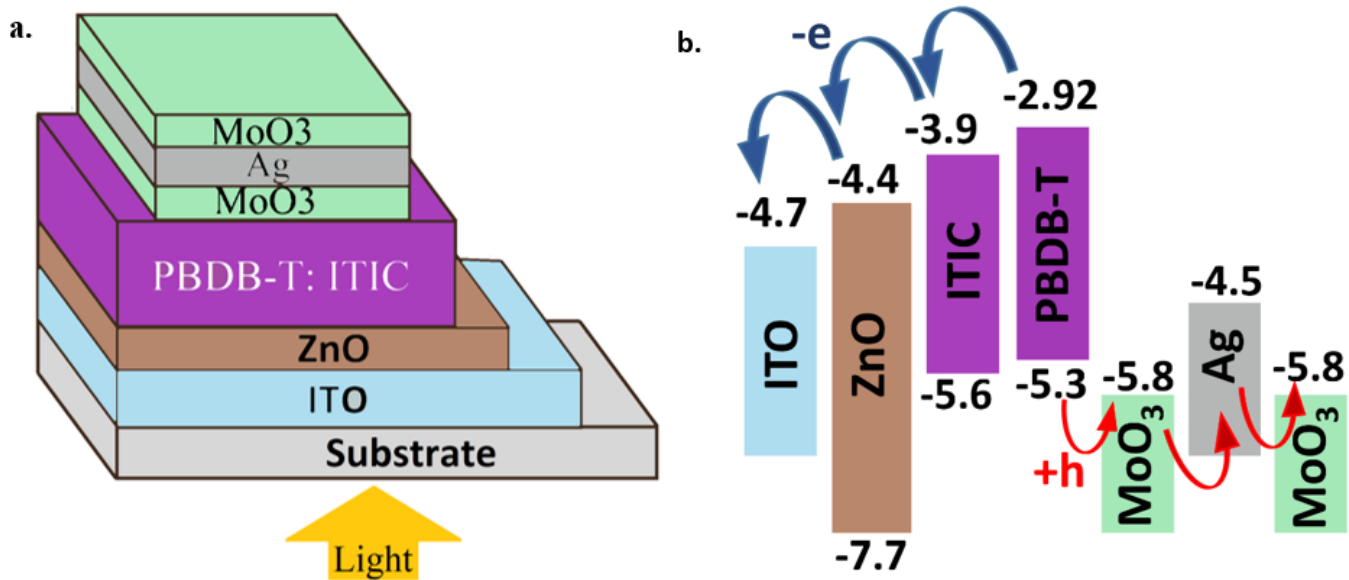


Figure 1

a. Schematic structure, b. The energy level diagram of the materials used in the ST-OSC studied structure.

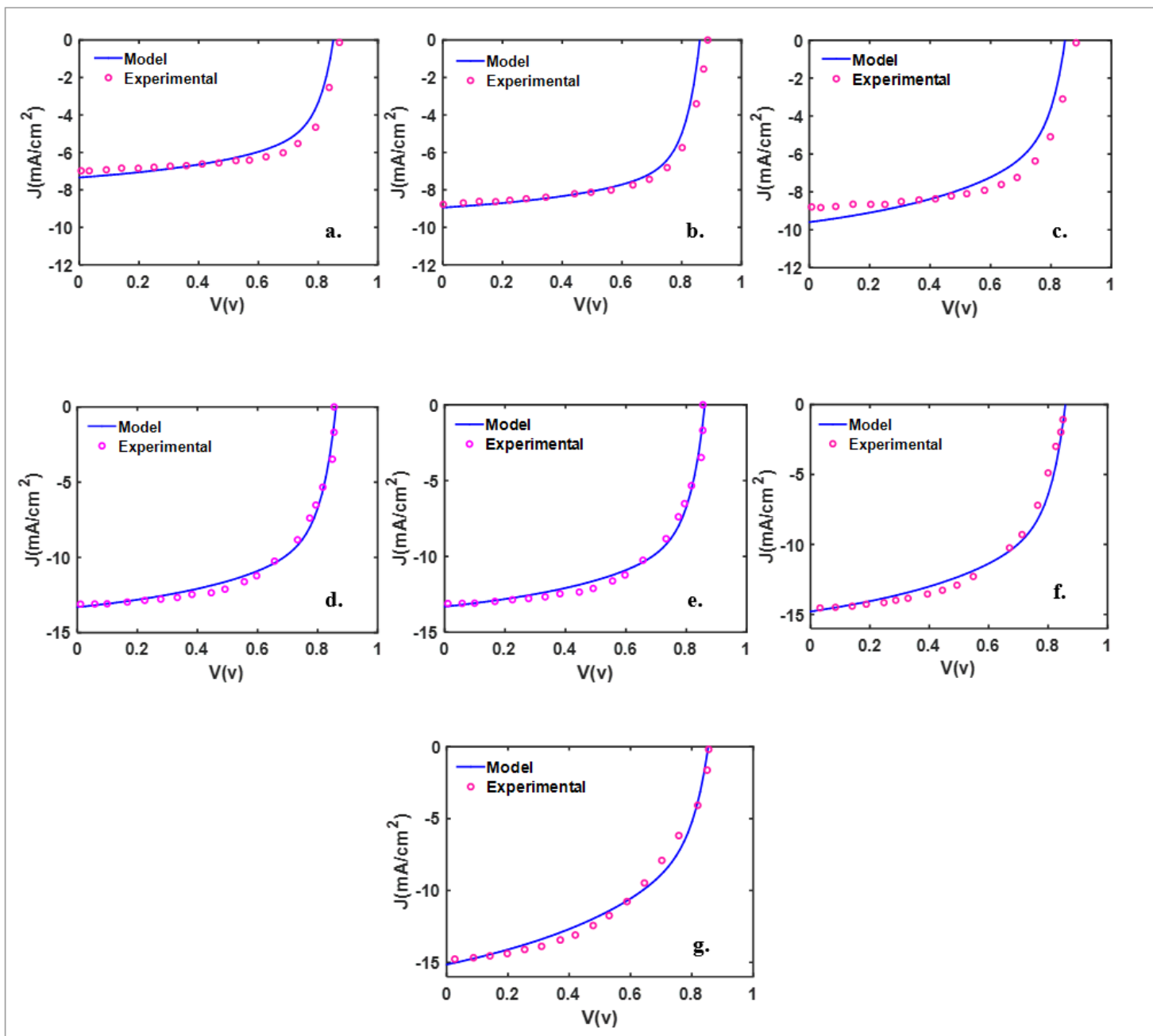


Figure 2

The J-V characteristics of the device with the structure of ITO/ ZnO/ PBDB-T: ITIC/ MoO₃/ Ag/ MoO₃, with D/M/D thickness of 10nm/6nm/30nm, and PBDB-T: ITIC active layer thickness is: **a.** 53, **b.** 59, **c.** 72, **d.** 91, **e.** 100, **f.** 114, **g.** 143 nm.

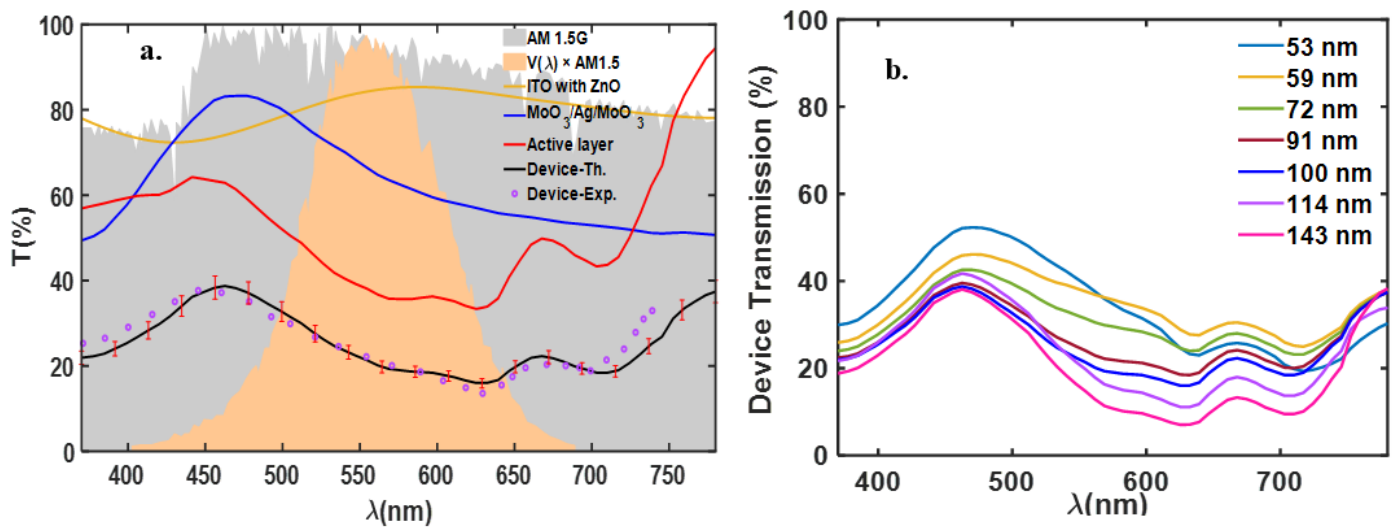


Figure 3

a. The calculated transmittance spectrum of the active layer (100nm), D/M/D, ITO with ZnO compact layer, the whole device, both theoretical (solid line) and experimental (dotted), AM1.5 spectral irradiance, and $V(\lambda) S_{\text{AM1.5}}(\lambda)$ **b.** The calculated transmittance spectrum of the devices for different active layer thicknesses.

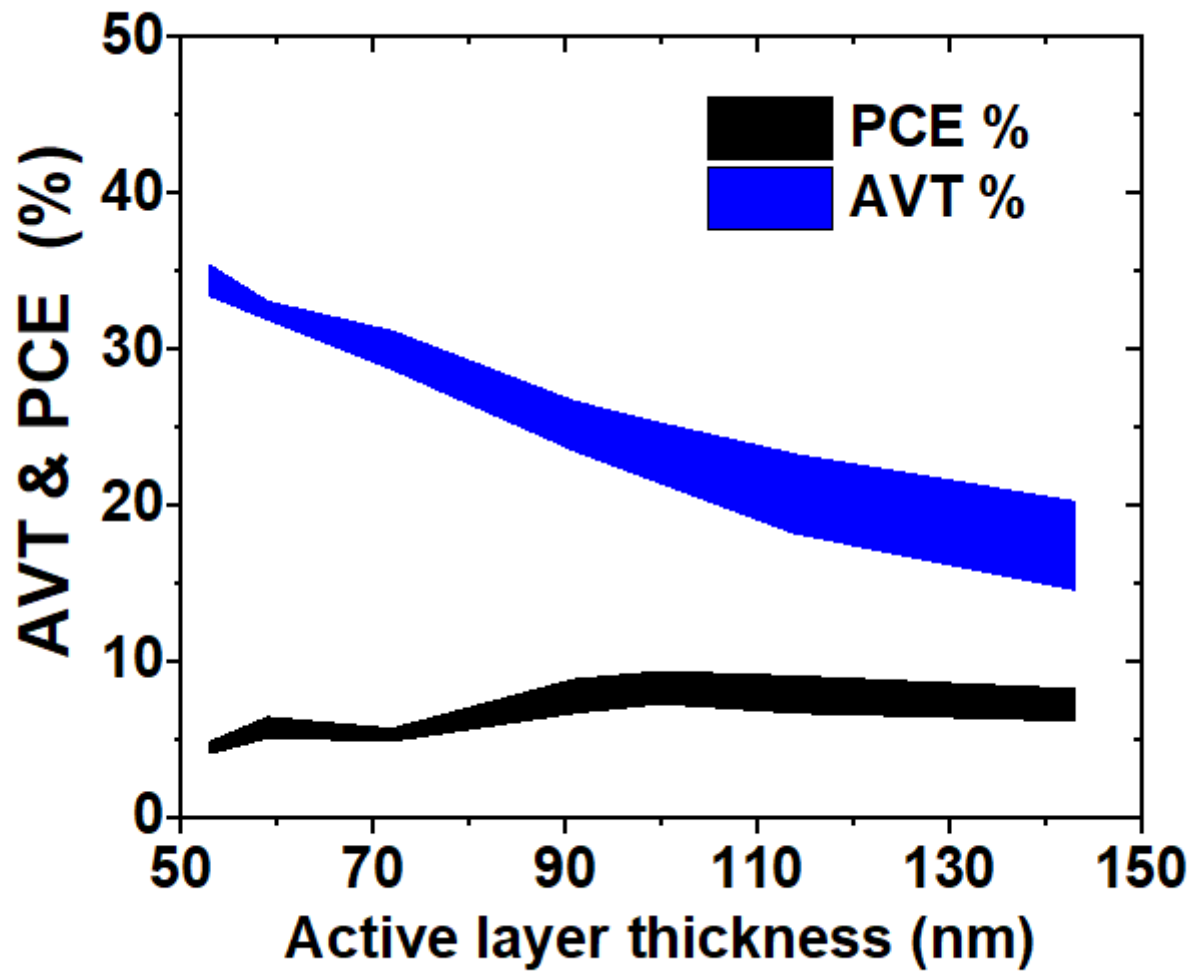


Figure 4

The PCE and AVT, as a function of active layer thickness. The filled area shows the difference between the experimental and theoretical data.

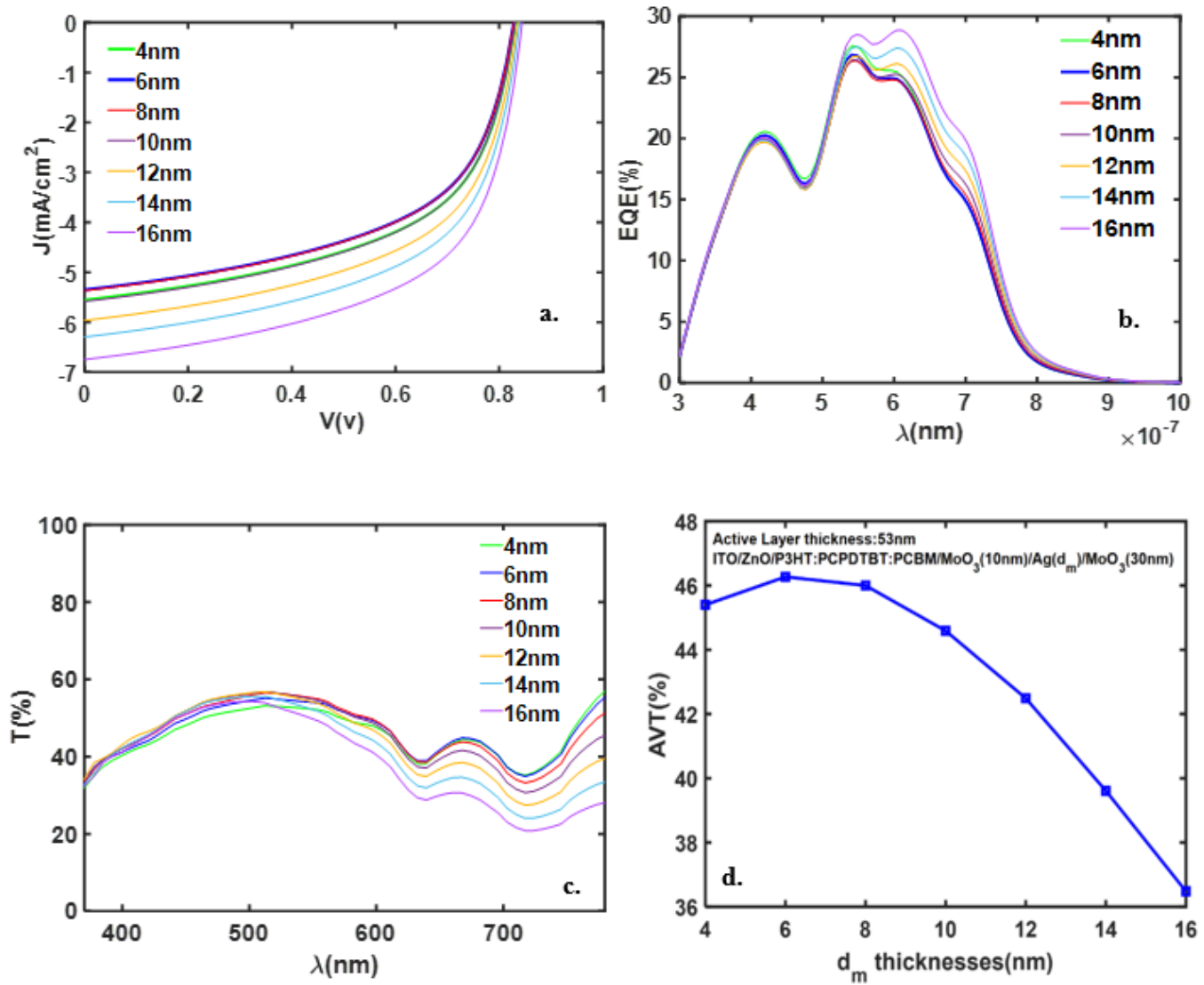


Figure 5

The J-V curve, **b.** the EQE as a function of wavelength, **c.** T as a function of the wavelength, **d.** the AVT as a function of d_m thicknesses for the devices with the active layer thickness of 53 nm.

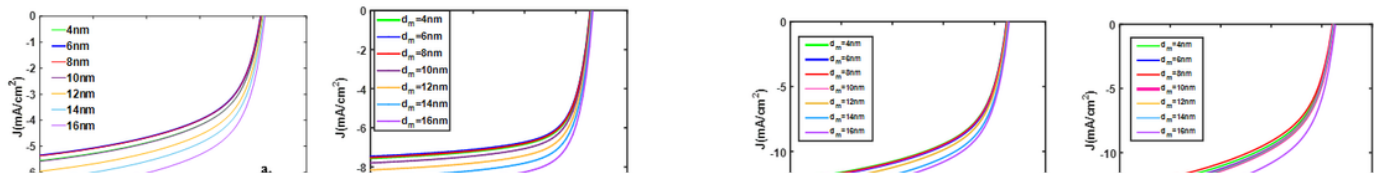


Figure 6

J-V curve for devices with a thickness of active layer **a.** 53nm, **b.** 59nm, **c.** 72nm, **d.** 91nm, **e.** 100nm, **f.** 114nm, **g.** 143nm, for various ' d_m ' thicknesses.

Figure 7

a. The J_{SC} , **b.** FF, and **c.** PCE (%) of the devices as a function of active and ' d_m ' layers thicknesses.

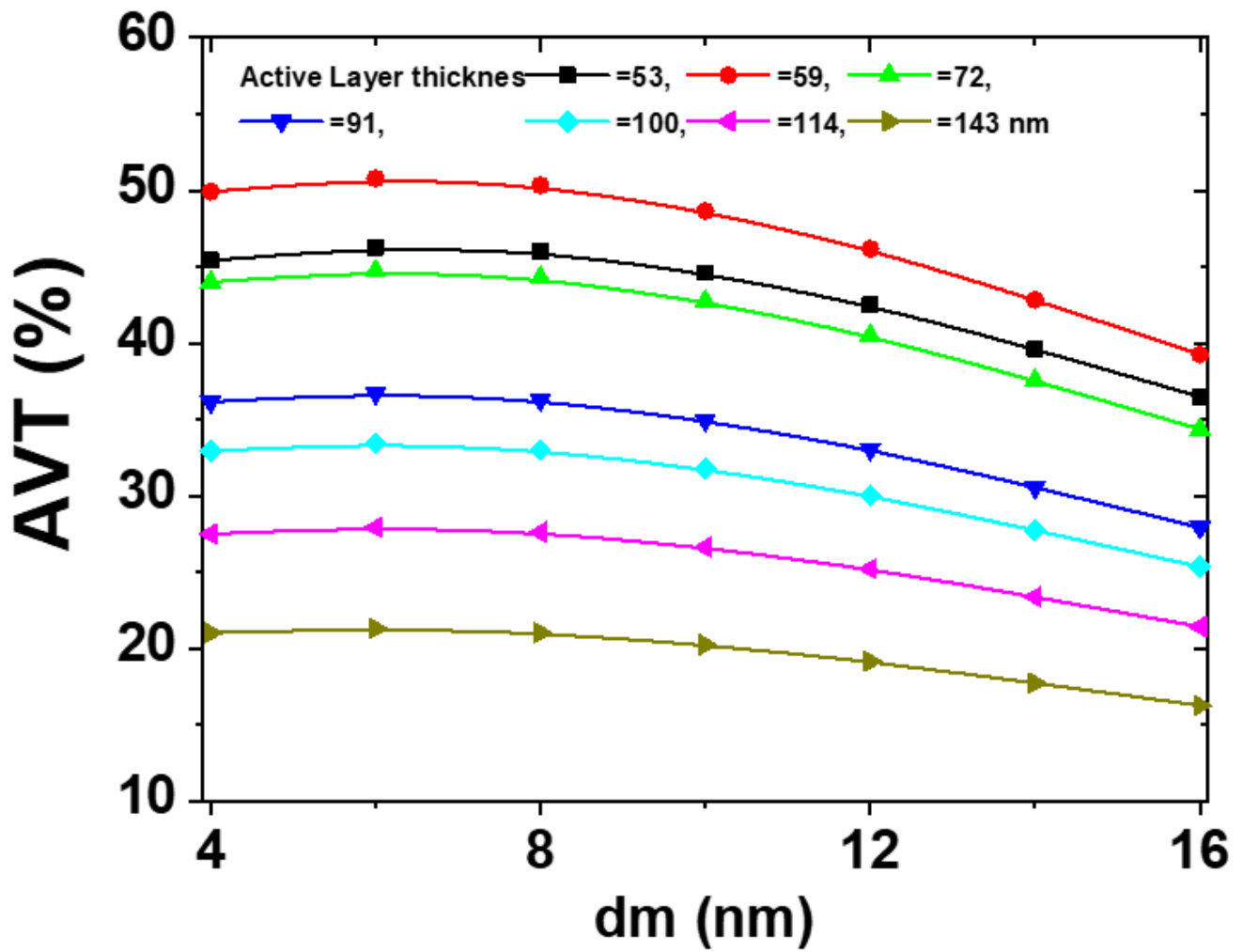


Figure 8

The AVT (%) of the devices as a function of active and ' d_m ' layers thicknesses.

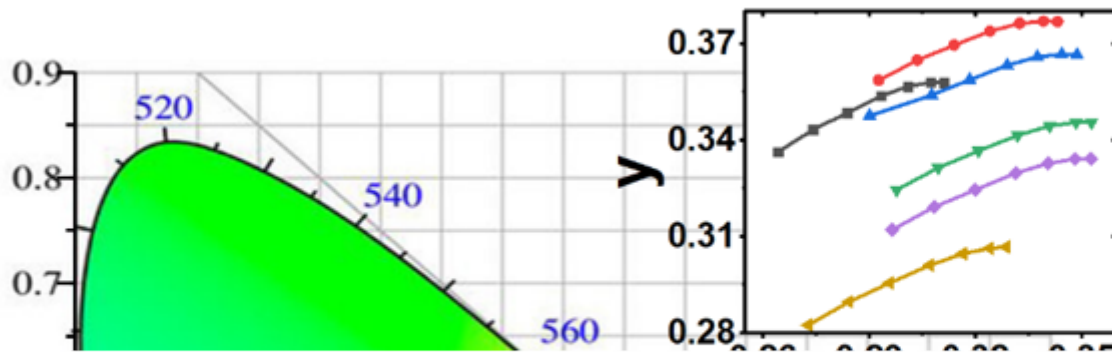


Figure 9

Representation of the color coordinate (x, y) of the ST-OSC with different active layers and d_m of D/M/D layer thicknesses, under standard D65 illumination light source on the CIE1931 color space